FABRICATION AND CHARACTERIZATION OF ELECTROCHEMICALLY FORMED NANOCRYSTALLINE POROUS Si AND GaAs

NIHAD KHALAF ALI
AL-OBAIDI

UNIVERSITI SAINS MALAYSIA

2008

FABRICATION AND CHARACTERIZATION OF ELECTROCHEMICALLY FORMED NANOCRYSTALLINE POROUS Si AND GaAs

by

NIHAD KHALAF ALI
AL-OBAIDI

Thesis submitted in fulfillment of the requirements
for the degree of
Doctor of Philosophy

June 2008

ACKNOWLEDGEMENTS

During the last few years which have brought me to the point where I am writing these acknowledgements, I have had the great fortune of receiving help in one form or other from many people. My advisor, Assoc. Prof. M. Roslan Hashim has guided me patiently through the latest part of my education as a PhD student. He has done this by always giving me time and sharing his abundance of knowledge. I am greatly indebted to him for the opportunity he gave me. Great thanks are also due to my second adviser, Assoc. Prof. Azlan Abdul Aziz for his continuous cooperation and guidance throughout my study.

I would like to express my gratitude to Assoc. Prof. Haslan Abu Hassan for his continuous and helpful support of my study. I am very grateful to Prof. Jamel Ismail for his encouragement, help and patience.

I would also like to express my appreciation to the staff in the Nano-Optoelectronics Research Laboratory for their co-operation, technical assistance, and valuable contribution to my work. The assistance from the staff of the Solid State Physics Laboratory is also acknowledged.

Finally, I dedicate this thesis to my family who has given me their unconditional support and encouragement.

Thanks to all.

TABLE OF CONTENTS

Acknowledgments	ii
Table of Contents	iii
List of Tables	vi
List of Figures	vii
List of Abbreviations	xii
List of Symbols	xiii
Abstrak	xiv
Abstract	xvi

CHAPTER 1 – INTRODUCTION

1.1	Overview	1
1.2	The Materials Science and History of Porous Silicon	5
1.3	Applications of Porous Silicon	9
1.4	Stability and Hardness of Porous Silicon	10
1.5	Porous GaAs	11
1.6	Objectives of the Thesis	13
1.7	Outline of the Thesis	14

CHAPTER 2 – PROPERTIES OF NANOSTRUCTURED MATERIALS

2.1	Introduction	15
2.2	Basic Principles of Bulk Semiconductors	15
2.3	Quantum Confinement in Nanostructured Materials	16
	2.3.1 Effective mass approximation	18
	2.3.2 Empirical pseudopotential method	22
	2.3.3 Tight-binding method	23
2.4	Light Emission from Silicon Nanostructures	23
	2.4.1 Shockley-Read-Hall recombination	24
	2.4.2 Auger recombination	25
2.5	Photoluminescence	27
	2.5.1 The IR-band	28
	2.5.2 The S-band	28

2.5.2(a) Surface species and molecules 29
2.5.2(b) Hydrogenated porous silicon 30
2.5.2(c) Surface states 30
2.5.2(d) Quantum confinement 31
2.5.3 The F-band 32
2.6 Synthesis of Porous Silicon 33
2.6.1 Electrochemical etching cell 35
2.6.2 Electrolyte properties 38
2.6.3 Etching procedure 39
2.6.4 Etching parameters 40
2.6.5 Drying 41
2.7 Mechanism of Silicon Dissolution and Pore Formation 42
2.8 Porous GaAs Formation Mechanism 47

CHAPTER 3 – POROUS SILICON SYNTHESIS AND CHARACTERIZATION
3.1 Introduction 50
3.2 Experimental Procedure 50
3.3 Relation between Current Density and Porosity 51
3.4 Relation between Etching Time and Thickness 54
3.5 Electrolyte Composition 56
3.5.1 Effect of electrolyte composition on porous surface morphology 56
3.5.2 Effect of electrolyte composition on porous surface chemistry 57
3.5.3 Effect of electrolyte composition on the light emission of porous silicon 61
3.6 Effects of Surface Passivation in Porous Silicon as H_2 Gas Sensor 62
3.7 Summary 67

CHAPTER 4 – POROUS SILICON FORMATION USING PULSED CURRENT METHOD
4.1 Introduction 68
4.2 Experimental Procedure 68
4.3 X-ray Diffraction 70
4.4 Raman Spectra 72

4.5 Photoluminescence Spectra 77
4.6 Improvement of Hardness and Stability of Porous Silicon 85
4.6.1 Methodology 86
4.6.2 Hardness measurements 87
4.6.3 Raman spectra 91
4.6.4 Photoluminescence spectra 93
4.7 Summary 95

CHAPTER 5 – SYNTHESIS AND CHARACTERIZATION OF HIGHLY LUMINESCENT n-TYPE POROUS GaAs
5.1 Introduction 96
5.2 Experimental Procedure 96
5.3 Surface Morphology 97
5.4 X-ray Diffraction 101
5.5 Raman Scattering 104
5.6 Photoluminescence Spectra 109
5.7 Synthesis and Characterization of n-Type Porous GaAs by Pulsed Current Electrochemical Anodization 114
5.7.1 Surface morphology 114
5.7.2 X-ray diffraction 117
5.7.3 Raman spectra 120
5.7.4 Photoluminescence spectra 121
5.8 Summary 124

CHAPTER 6 – CONCLUSIONS AND FUTURE OUTLOOK
6.1 Conclusions 125
6.2 Future Outlook 128

REFERENCES 129
LIST OF PUBLICATIONS 147

LIST OF TABLES

Page

Table 4.1 Schematic of the energy bands structure of GaAs and Si, the arrow indicates the lowest energy transition [After Blakemore 1985]. **69**

LIST OF FIGURES

		Page
Figure 2.1	Schematic of the energy bands structure of GaAs and Si, the arrow indicates the lowest energy transition [After Blakemore 1985].	**16**
Figure 2.2	Schematic of the low-dimensional structure and the density of state (DOS) as a function of the energy for a particle controlled to move in the bulk (a), in a quantum well (b), in quantum wire (c), and quantum dot (d) [After Hens *et al.* 2002].	**17**
Figure 2.3	Effective mass approximation consists of quadratic fit to the valence maximum and conduction minimum [After Lockwood *et al*. 1996].	**19**
Figure 2.4	Schematic diagram of a quantum mechanical system by a particle of mass m confined in a one-dimensional box of length *a*. For the particle to be confined within region II, the potential energy outside (regions I and III) is assumed to be infinite [After Das and Melissinos 1986].	**21**
Figure 2.5	Confinement within nano-sized crystalline cause's enlargement in the band gap energy, with respect to the bulk crystal.	**22**
Figure 2.6	Radiative and non-radiative recombination processes in semiconductors [After Tamor and Wolfe 1980].	**25**
Figure 2.7	Schematic drawing of a conventional single-tank cell, two silicon electrodes were used; one act as an anode, where the porous layer formed, and the second one act as a cathode.	**36**
Figure 2.8	Schematic drawing of a conventional single-tank cell. The silicon wafer acts as an anode while a platinum grid as a cathode.	**37**
Figure 2.9	Schematic drawing of a double-tank anodizing cell.	**38**
Figure 2.10	Suggested mechanism for the electrochemical dissolution of silicon [After Lehmann and Gösele 1991].	**45**
Figure 3.1	Scanning electron microscopy (SEM) images of porous silicon. The dark regions are the void space and the bright matrix is silicon. The pore size and morphology can be tuned (as shown in the images) by changing the applied current density.	**52**
Figure 3.2	Relation between porosity and current density.	**53**
Figure 3.3	SEM cross section images of PS samples etched with different anodizing time, the thickness increases as the etching time increases.	**54**

Figure 3.4 Relation between the anodization time and the thickness of the porous layer, obtained for two different current densities. **55**

Figure 3.5 Relation between the applied current density and the etch rate of porous silicon layer. **55**

Figure 3.6 SEM images of PS samples: a) anodized in HF:ethanol, 1:4, (b) anodized in HF: ethanol: hydrogen peroxide (H_2O_2), 1:2:2. **57**

Figure 3.7 FTIR spectra of the PS samples; (HF) prepared with HF: ethanol, (1:4) and (HF:H_2O_2) prepared with HF: ethanol: hydrogen peroxide (H_2O_2), (1:2:2). **59**

Figure 3.8 FTIR spectra of PS samples; (HF) prepared in HF: ethanol, 1:4, current density of 20 mA/cm^2, samples (HF:H_2O_2), and (2HF:H_2O_2) prepared in HF:H_2O_2: ethanol, 1:2:2, current density of 20 mA/cm^2, and 50 mA/cm^2, respectively. **60**

Figure 3.9 PL spectra of PS samples; (HF) prepared in HF:ethanol, 1:4, current density of 20 mA/cm^2, samples (HF:H_2O_2), and (2HF:H_2O_2) prepared in HF:H_2O_2:ethanol, 1:2:2, current density of 20 mA/cm^2, and 50 mA/cm^2, respectively. **61**

Figure 3.10 Gas chamber for testing PS as a sensor. **63**

Figure 3.11 I-V curves of Al/PS/p-Si (with H_2O_2) for different H_2 concentrations at room temperature. **64**

Figure 3.12 Current sensitivity versus hydrogen concentration of Al/PS/p-Si prepared using anodizing solution a) without H_2O_2 b) with H_2O_2. Also included is the characteristic for non porous Al/p-Si for comparison. **65**

Figure 3.13 I-V characteristics of Al/PS/p-Si (with H_2O_2) exposed to 10% H_2 measured at different temperatures. **67**

Figure 4.1 Schematic diagram of wave form of the pulse current used in the etching process. **69**

Figure 4.2 XRD spectrum of bulk silicon. **70**

Figure 4.3 XRD spectra of PS samples anodized with a) constant current density of 5 mA/cm^2 (thick line), 15 mA/cm^2 (thin line), b) pulsed current density of 15 mA/cm^2 pause time 2 ms (thick line) and 7 ms (thin line). **71**

Figure 4.4 Raman spectra of p-type PS samples. The solid lines are the experimental data and the dotted lines are the generated spectra using quantum confinement model. **73**

Figure 4.5 Raman spectra of n-type PS samples. The solid lines are the experimental data and the dotted lines are the generated spectra using quantum confinement model. **74**

Figure 4.6 The relationship between the red shift from that of c-Si and the linewidth. The dots represent the experimental data, the solid line is drawn to guide the eye, and the dashed line is the calculated results using the three dimensional phonon confinement model. **77**

Figure 4.7 PL spectra for samples anodized with constant current density of (a) 15 mA/cm^2 (dc1) and (b) 5 mA/cm^2 (dc2). **78**

Figure 4.8 PL spectra for p-type PS samples anodized with pulsed current density of 15 mA / cm^2, duration time T of 175 ms with different pause time T_{off}, 2 ms (T_{off}2), 4 ms (T_{off}4), 5 ms (T_{off}5) and 7 ms (T_{off}7). Sample (dc1) anodized with direct current density of 15 mA/cm^2. **79**

Figure 4.9 PL spectra for p-type PS samples anodized with pulsed current density of 5 mA / cm^2, duration time T of 140 ms with different pause time T_{off}, : (5T_{off}1) 1 ms, (5T_{off}5) 5 ms, (5T_{off}11) 11 ms, and (5T_{off}13) 13 ms. Sample (dc2) anodized with constant current density of 5 mA/cm^2. **80**

Figure 4.10 PL spectra for n-type PS samples anodized with pulsed current density of 15 mA / cm^2, duration time T of 140 ms with different pause time T_{off} samples (T_{off}12) 12 ms, (T_{off}25) 25 ms, (T_{off}50) 50 ms, and (T_{off}75) 75 ms respectively. Sample dc anodized with constant current density of 15 mA/cm^2. **81**

Figure 4.11 Correlation between PL spectral peak (energy gap) and crystallite size of PS. Theoretical values of Brus (1984) and Kayanuma (1988) (solid line), and our experimental data; filled triangles for n-type and unfilled triangles for p-type. **83**

Figure 4.12 Compilation of optical band gaps of silicon crystallites and porous silicon samples obtained from optical absorption (unfilled circles, Lockwood 1994) and luminescence (filled circles, Schuppler *et al.* 1994), and also the results of Ehbrecht *et al.* (1997) (unfilled rectangles). Dashed and continuous lines: calculated values of Proot *et al*. (1992) with and without the excitonic correction. Theoretical values of Brus (1984) and Kayanuma (1988) (solid line), and our experimental data filled triangles for n-type and unfilled for p-type. **84**

Figure 4.13 Surface SEM images of capped porous samples (a), (b), and (c) and their cross section images showing the silicon cap thickness upon the porous silicon layer. **87**

Figure 4.14	Indentation on a porous silicon capped samples (a), (b), and (c) surface using load of 0.245, 0.49, 0.98, and 1.96 N.	**89**
Figure 4.15	Vickers hardness as a function of silicon cap thickness and for as anodized porous silicon. Usual value of crystalline silicon is also shown as horizontal bar, indicating the hardness level.	**90**
Figure 4.16	Raman spectra of capped porous silicon samples (a), (b), and (c), also included the spectra of as anodized porous silicon sample and crystalline silicon for comparison.	**92**
Figure 4.17	PL spectra of an as-anodized porous silicon layer, capped porous silicon samples (b) and (c). The spectra taken of as prepared sample, after 2 weeks, and after 2 months.	**94**
Figure 5.1	The typical SEM images of π-GaAs investigated samples; (a), (b), (c), and (d) show the surface morphology, while images a^-, b^-, c^-, and d^- shows the cross section.	**98**
Figure 5.2	Top view SEM images of π-GaAs sample etched with HCl solution (sample HCl) at different magnifications from three different regions.	**100**
Figure 5.3	SEM micrograph of a π-GaAs sample showing the As_2O_3 and/or Ga_2O_3 single crystals formed on the sample surface.	**101**
Figure 5.4	XRD spectra of π-GaAs samples; (a), (b), and (c) anodized with HF:Ethanol electrolyte, current density of 5, 10, and 15 mA/cm^2, respectively, and sample (HCl) anodized with 1 M HCl solution, current density of 15 mA/cm^2.	**103**
Figure 5.5	Raman spectra of c-GaAs and π-GaAs samples ((a), (b), and (c)) etched with HF based solution, current density of 5, 10, and 15 mA/cm^2, respectively for 30 min.	**105**
Figure 5.6	Raman spectra of c-GaAs and π-GaAs sample etched with HCl based solution, taken from different regions.	**107**
Figure 5.7	Raman spectra of π-GaAs sample etched with HCl based solution taken from different regions. The solid lines are the experimental data. The doted lines are the generated spectra using quantum confinement model. Also plotted is the Raman spectrum of c-GaAs for comparison.	**109**
Figure 5.8	The PL spectra of c-GaAs and π-GaAs samples ((a), (b), and (c)) formed with different current densities of 5, 10, 15 mA/cm^2, respectively for 30 min in HF based solution.	**110**

Figure 5.9 The PL spectra of c-GaAs and π-GaAs sample etched with HCl based solution taken from different regions. **112**

Figure 5.10 SEM images show the surface morphology of π-GaAs samples; (T_{off}10), (T_{off}20), (T_{off}40), and (T_{off}60) prepared using pulse current and sample (dc) prepared using direct current, while images a^-, b^-, c^-, d^- and dc^- show the cross sections. **115**

Figure 5.11 The EDX analysis of the π-GaAs layer for samples prepared with pulse and direct currents; Ga% and As% versus T_{off}, (T_{off} = 0) represents sample (dc). **117**

Figure 5.12 XRD spectra of π-GaAs samples; (T_{off}10), (T_{off}20), (T_{off}40), and (T_{off}60) anodized with pulsed current at peak current density of 10 mA/cm^2, with cycle time of 140 ms and T_{off} of 10, 20, 40, and 60 ms, respectively. Sample (dc) was prepared by dc current of 10 mA/cm^2. **118**

Figure 5.13 XRD spectra of π-GaAs samples; a) anodized with pulsed current at peak current density of 10 mA/cm^2, with cycle time of 140 ms and T_{off} of 40 ms, b) sample (dc) was prepared by dc current of 10 mA/cm^2. **119**

Figure 5.14 Raman spectra of π-GaAs samples (T_{off}10), (T_{off}20), (T_{off}40), and (T_{off}60) which were etched by pulsed current at the peak current density of 10 mA/cm^2, cycle time of 140 ms, and off time, T_{off} of 10, 20, 40, and 60 ms, respectively, while sample (dc) was prepared by direct current anodic etching with the current density of 10 mA/cm^2. **121**

Figure 5.15 PL spectra taken from π-GaAs samples (T_{off}10), (T_{off}20), (T_{off}40), and (T_{off}60) which were etched by pulsed current at peak current density of 10 mA/cm^2, with cycle time of 140 ms, and off time of 10, 20, 40, and 60 ms, respectively. Sample (dc) etched with direct current of 10 mA/cm^2. **123**

LIST OF ABBREVIATIONS

PS	porous silicon
π-GaAs	porous gallium arsenide
HF	hydrofluoric acid
T	cycle time
T_{off}	pause time
T_{on}	time on
XRD	X-ray diffraction
SEM	scanning electron microscopy
FT-IR	fourier transform infrared
nc-Si	nanocrystalline Si
c-Si	single crystalline silicon
PL	photoluminescence
VLSI	very-large-scale integration
FIPOS	full isolation by porous oxidized silicon
TC	thermal conductivity
DOS	density of state
EMA	effective mass approximation
TB	tight-binding
SRH	shockley-read-hall
P	porosity
J	current density
S	sensitivity
W	depletion width
RT	room temperature
FWHM	full width half maxima
LEPS	light-emitting porous silicon
HV	vickers hardness number
F	load
D	indentation depth
LO	longitudinal optical
TO	transverse optical

LIST OF SYMBOLS

m^*	effective mass of the charge carrier
m_e	electron effective mass
m_h	hole effective mass
k	wavevector
a	width of the potential well
ηi	internal quantum efficiency
ρ	silicon density
S	surface area
2θ	diffraction angle
L	diameter or size of Si nanocrystallite
Γ_c	full width half maxima of Si nanocrystallite
$\omega_{LO}(q)$	longitudinal phonon frequency at q
q	wave vector
E^*_{Ry}	effective Rydberg energy
ε_r	dielectric constant
a_{PS}	lattice constant of porous silicon
t	film thickness

FABRIKASI DAN PENCIRIAN HABLUR NANO Si DAN GaAs YANG DIBENTUK OLEH ELEKTROKIMIA

ABSTRAK

Bahan hablur nano berjalur tenaga terus dan tak terus (poros silicon, PS dan poros GaAs, π-GaAs) telah difabrikasi dan ciri-ciri optic mereka telah dikaji dengan mendalam. Dalam penyelidikan ini, dua pendekatan fabrikasi telah digunakan. Pertama, menggunakan kaedah konvensional, anodisasi elektrokimia arus malar di dalam sebatian HF, pelbagai rupabentuk permukaan dan darjah keporosan telah diperolehi. Keputusan menunjukkan bahawa darjah keporosan meningkat secara songsang dengan kepekatan HF dan secara terus dengan ketumpatan arus. Ketebalan lapisan poros meningkat dengan masa punaran. Komposisi elektrolit juga mengubah ciri-ciri PS. Kami telah menyediakan PS dengan memasukkan peroksida (H_2O_2) dalam sebatian punaran. Sampel yang dianodisasi dengan peroksida menghasilkan struktur PS dengan darjah keporosan yang tinggi (~80%) dan passivasi permukaan yang lebih baik (kepekatan Si-O dan Si-H yang lebih tinggi) berbanding dengan sampel tanpa peroksida. Sampel yang menggunakan peroksida yang telah dibina sebagai pengesan gas H_2 menunjukkan kesensetifan elektrik (I-V) yang lebih tinggi berbanding dengan sampel tanpa peroksida disebabkan oleh passivasi permukaan yang lebih baik dan saiz hablur yang lebih kecil. Passivasi permukaan juga tidak berubah banyak walaupun pada suhu yang lebih tinggi (100°C).

Pendekatan kedua menyediakan PS ialah melalui teknik baru iaitu punaran menggunakan arus denyut (ulang alik). Sampel yang boleh memancarkan sinar pelbagai jarak gelombang telah berjaya disediakan dimana jarakgelombang bergantung kepada masa kitaran (T) dan masa henti (T_{off}) arus denyut tersebut semasa proses punaran. Sifat-sifat struktur nano telah ditunjukkan melalui Diffraksi sinar-X (XRD) dan disahkan oleh fotoluminesen (PL) dan spektroskopi Raman. Keputusan PL dari sampel PS punaran arus denyut menunjukkan jarakgelombang pancaran yang berbagai dengan keamatan yang tinggi. Keputusan dari serakan Raman berkenaan fonon optik di dalam PS menunjukkan anjakan-merah bagi frekuensi fonon, pelebaran spektrum dan peningkatan ketaksemetrian mod Raman dengan peningkatan T_{off}. Menggunakan model terkurung fonon, diameter purata

hablur nano Si telah dianggarkan antara 3-5 nm untuk PS jenis-p dan antara 2-4 nm untuk PS jenis-n. Kedua-dua keputusan Raman dan PL mencapai persetujuan yang sangat baik dan diterangkan menggunakan model-model terkurung kuantum. Dalam penyelidikan ini, kaedah untuk memperbaiki kestabilan sturktur PS juga dilakukan dengan endapan penutup silicon secara elektrokimia. Keputusan menunjukkan hubungan linear antara ketebalan lapisan penutup dengan masa endapan.. Juga kekerasan Vickers telah meningkat dari 1.2 ke 2.9 Gpa untuk beban sebanyak 0.49N dengan peningkatan ketebalan penutup dari 0 (tanpa penutup) kepada 7 μm dan spectrum PL yang stabil diperolehi.

Penyelidikan ini juga menyediakan π-GaAs melalui punaran keatas wafer GaAs jenis-n di dalam larutan HF atau HCl. Keputusan utama menunjukkan GaAs jenis-n dalam larutan HCl menghasilkan struktur poros yang tidak seragam. Darjah keporosan membahagikan sampel kepada tiga kawasan yang berlainan. Sampel dikaji menggunkan teknik Raman dan PL. Keputusan menunjukkan pancaran spontan dari kesemua rantau ini berasal dari struktur-struktur yang kecil. Bila darjah keporosan meningkat, puncak luminesen juga meningkat, anjakan Raman ke paras tenaga yang lebih rendah, mempamerkan pelebaran spektrum dan penurunan keamatan puncak mod optik membujur turutan-pertama. Kedua-dua keputusan Raman dan PL bersetuju antara satu sama lain dan telah diterangkan menggunakan model terkurung kuantum. Teknik punaran elektrokimia arus denyut juga telah digunakan untuk menghasilkan π-GaAs. Keputusan menunjukkan bahawa penghasilan lapisan π-GaAs digalakan melalui pembentukan dan pelarutan lapisan oksida bergantung kepada T_{off} . Diffraksi sinar-X menunjukkan kualiti saiz hablur yang lebih baik berbanding dengan sampel menggunakan kaedah biasa (arus terus). Spektrum PL pada suhu bilik menunjukan kewujudan dua atau tiga puncak PL di samping puncak yang disebabkan dari hablur tunggal GaAs; iaitu pada 362, 426, dan 540 nm.

FABRICATION AND CHARACTERIZATION OF ELECTROCHEMICALLY FORMED NANOCRYSTALLINE POROUS Si AND GaAs

ABSTRACT

Indirect and direct band gap nanocrystalline materials (porous silicon, PS and porous GaAs, π-GaAs) have been fabricated and their optical properties were extensively studied. In this work, two approaches to manufacture these materials are employed. First approach, we prepared PS using conventional method of constant current electrochemical anodization in HF based solution. Our results showed that; porosity increases inversely with HF concentration and directly with current density. Layer thickness increases linearly with etch duration. Electrolyte composition also alters the characteristics of PS. We prepared PS by incorporating the highly oxidant H_2O_2 in the anodizing process. Our results showed a PS structure with higher porosity (~80%) and better surface passivation (higher concentration of Si-O and Si-H species) compared to those not treated with peroxide. The peroxide based PS sample fabricated as an H_2 gas sensor showed better electrical (I-V) sensitivity compared to those without peroxide due to better surface passivation and smaller crystallite size. Surface passivation in peroxide based PS is also maintained at higher temperatures (100°C).

The second approach to prepare PS was to use a new technique based on pulsed current anodic etching. Samples with selective wavelength emission have been prepared using this technique depending on cycle time (T) and pause time (T_{off}) of pulsed current during the etching process. Nanostructural nature of the porous layer has been demonstrated by X-ray diffraction (XRD) analysis and confirmed by photoluminescence (PL) and Raman spectroscopy. PL measurements of pulsed anodic etching PS showed variety of emission wavelengths with strong intensity. Our results on Raman scattering from the optical phonon in PS showed the redshift of the phonon frequency, broadening and increased asymmetry of the Raman mode with increasing T_{off}. Using the phonon confinement model, the average diameter of Si nanocrystallites has been estimated. The estimated Si nanocrystallite sizes obtained are 3-5 nm for p-type PS samples and 2-4 nm for n-type PS layers. Both Raman and

PL results were in good agreement and explained using quantum confinement models. In this work we also presented a method to improve the stability of PS structure by electrochemical deposition of silicon capping. Our results showed a linear relation between capping layer thickness and the deposition time. Vickers hardness has been shown to increase from 1.2 to 2.9 Gpa for an applied load of 0.49N with increasing capping layer thickness from 0 (without capping) to 7 μm, respectively, and stable PL was obtained.

We prepared π-GaAs by electrochemical etching of n-type GaAs wafers in HF or HCl-based solution. Our results showed that the central feature of anodic processing of n-type GaAs in aqueous HCl electrolyte is a nonuniform porous structure. By the porosity, three different regions were identified. The samples were subjected to Raman and PL spectroscopic investigations. Our results showed that the spontaneous emission of these structures is originated from extremely small structures. As the porosity increases, there is an increase of the luminescent peak, lower energy shifting of the Raman feature, exhibiting broadening and decreased of first-order longitudinal optic mode peak intensity. Both Raman and PL results have been explained using quantum confinement models, and showed a reasonable agreement between the two techniques. We also used the pulsed current electrochemical etching technique to prepare π-GaAs. Our results showed that the formation of π-GaAs layers using this technique has been promoted through the formation and dissolution of oxide layer depending on T_{off}. X-ray diffraction (XRD) shows higher quality crystal size compared to those of direct current. Room temperature photoluminescence (PL) investigations reveal the presence of two and in some cases three PL bands besides the PL band of the single crystalline GaAs (c-GaAs): located at 362, 426, and 540 nm.

CHAPTER 1

INTRODUCTION

1.1. Overview

Today, an enormous quantity of information is passed between computers through optical fibers and across wireless telephones. The end user demands that the information be transferred quickly. In the last two decades, the field of microelectronics has undergone a strong development, concerning higher and higher integration density, and lower fabrication costs. Microelectronic devices currently face a considerable challenge providing the necessary communication between computer's boards, chips and even individual chip components. This creates an interconnect bottleneck, which is predicted to become a "grand challenge" for the semiconductor industry by the year 2018 (International technology roadmap for semiconductors, 2007). For intra-chip interconnections, the "bottleneck" can be traced back to a combined effect of two problems: the spatial density problems (leading to a higher integration density) and the signal speed problem (requesting the use of higher frequency).

There are several possible approaches to such interconnection scaling problems; architectures could be changed to minimize interconnections. Signaling on wires could be significantly improved through the use of a variety of techniques (Collet *et al.*, 2001; Kochar *et al.*, 2007). Additionally, to further increase speed and performance in electronic devices, feature size must continue to decrease. As feature size continues to scale down, quantum effects, such as tunneling and carrier confinement, are no longer negligible. Furthermore, small features require exotic and

costly lithographic techniques (Corbett *et al*., 2000; Chas, 2001). But consumers require that electronics be cheap. Hence, scientists and engineers are faced with some interesting challenges.

In order to maintain the rate of advancement of high-speed and efficiency of device performance, alternative technologies need to be investigated. Adding optical functionality to existing electrical capabilities is one option for enabling enhanced device operation. It is widely believed that optical interconnects will begin replacing many copper connections within the next decade (Savage, 2002). In fact, as it is known, using light in optical fibers for communication systems would allow us to speed up the information flux, since optical signals travel at the light speed, without any reciprocal influences. As a consequence the interest of the present technological research strongly focused on optical approaches. One solution is the integration of wireless, or optical, interconnects with silicon ultra large-scale integration.

Silicon (Si), one of the base elements of our planet, is the foundation of the modern information society. Integration and economy of scale are the two key ingredients in the technological success of Si. Modern electronics would be unthinkable without the development of silicon transistors. These silicon transistors are made possible only by the outstanding characteristics and stability of silicon and its oxides. However, the increasing miniaturization of microelectronics, the demands of optoelectronics, and the development of optical communication technology bring the limits of silicon technology. Unfortunately, the development of Si-based photonics has lagged far behind the development of electronics for a long time. This is because it is an indirect band gap semiconductor, in which radiative transition results in extremely weak light emission in the infrared part of the spectrum (1.1 eV) in its bulk form. For future applications on optoelectronic interconnect it is necessary

to have a material in which light can be generated, guided, modulated, amplified and detected. While reasonable advances have been made for on-chip waveguides and detectors, modulators remain the key obstacle inhibiting the realization of optical interconnects (Chen *et al*., 2007). Moreover, the development of a silicon-based on-chip light source would be valuable assets to reduce interconnect cost and complexity. Thus, the light emitting structures mostly used in optoelectronics are based on the III-V elements such as gallium arsenide (GaAs) or indium phosphide (InP) or combinations of them which are not compatible with silicon (Corbett *et al*., 2000). The hybrid approach, i. e. the integration process of III-V semiconductors into silicon chips, is quite difficult and very expensive for the microelectronic industry. Another way to develop a silicon-based on-chip light source is to turn Si into nanostructure material.

Nanostructure materials are another path to prepare new materials with excellent optical and electrical properties; they are a truly new form of matter that can be considered as “artificial atoms”. Nanostructure materials may be defined as those materials whose structural elements-clusters, crystallites or molecules have dimensions in the 1 to 100 nm range, they are mostly called quantum dots. A wide class of semiconductor materials can now be prepared in nanocrystal, quantum dots form including: covalent Si and Ge (Voigtl *et al*., 2004), III-V compounds (GaAs, InP, GaN) (Li *et al.,* 2000; Liu and Duan, 2001a; Takeda *et al.,* 2005), II-VI (CdSe) (Lohmeyer *et al.*, 2006), and I-VII compounds (Hwanga *et al.*, 2006). As a result, instead of 109 elements, we have in principle, an unlimited number of “atomic elements” to form new materials.

The nanocrystal size and shape are practically the only two parameters that govern optical transition energies. The energy gap between valence and conduction

band is of fundamental importance for the properties of semiconductors. Most of a material's behavior, such as intrinsic conductivity, optical transitions, or electronic transitions, depends on it. Any change of the gap may significantly alter the material's physics and chemistry (Bechiria *et al*., 2003). This occurs when the size of a bulk is reduced to the nanometer length scale below the Bohr exciton radius of the semiconductor, hence quantum confinement effects arises. Therefore, the science and the technology of nanomaterials need to take into account a band gap, which is different from that of the bulk (Sattler, 2003). In a bulk semiconductor material, electrons are free to move in any of the three spatial directions, while, quantum structures confine the mobility of electrons. Quantum structures exhibit interesting variations in their properties at sizes of about 10 nm and below (Photopoulos and Nassiopoulou, 2003). A confining structure may be made by embedding a limited region of one material within another (e. g., Si with SiO_2) (Kohli *et al.*, 2004). The difference between allowed electronic states for the two materials forms a barrier to free electron movement.

In view of that, structures in nanometer range provide a solution since silicon manifests different characteristics in the nanoscale regime. In a range of very few nanometers, the movement of electrons and electron vacancies in silicon is narrowly restricted, so quantum confinement effects (Wilson *et al*., 1993) appear which enlarge the band gap of silicon and shift the light emission into visible range by breaking the momentum conservation rule. Silicon nanocrystals research is focused on the preparation of Si nanocrystals embedded in an oxide host (Cazzanelli *et al*., 2004). Methods applied for preparation of Si nanocrystals are Si ion implantation into high quality oxides (Tsutomu, 1999), sputtering of Si rich oxides (Mas *et al*., 2001), or reactive evaporation of Si rich oxides (Zhang *et al*., 1998). The size control

is realized in all these methods by changing the chemical stoichiometry of the films. Reduction of the implanted Si dose or the oxygen enrichment is the usual ways for a decrease in nanocrystal size. However, by decreasing the nanocrystal size into the desired range, the density of the nanocrystals is reduced simultaneously (Feng *et al*., 2005). In addition, there is only limited control of size distribution. Research on the preparation of nanocrystalline Si (nc-Si) is pioneered by the work on porous silicon (PS) which shows that when silicon is partially etched in an HF solution via an electrochemical attack, the surviving structure is formed by small nanocrystals or nanowires shows bright red luminescence at room temperature (Canham, 1990).

With regard to a strong photoluminescence (PL) of the nc-Si in the visible spectral range the control of size, passivation, and density is mandatory. A blueshift of the luminescence is observed with decreasing nanocrystal size. In fact, the first success in the improvement of the silicon emission properties was the discovery of efficient light emission in PS where nc-Si is formed and quantum confinement of photo excited carriers yields to a band-gap widening and an increased transition rate (Canham, 1990). These observations have promoted a wide interest worldwide with the development of many other low-dimensional silicon based system.

1.2. The Materials Science and History of Porous Silicon

Of all the types of nanoscale Si, porous silicon has received the most attention to date. Porous silicon can be considered as a silicon crystallite having a network of nanosized voids in it. The nanosized voids in the bulk silicon result in a sponge-like structure of pores and channels surrounded with a skeleton of crystalline Si nanowires. Described simply, PS is a network of air holes in a silicon matrix. Porous silicon was discovered in 1956 by Uhlir while performing electropolishing

experiments on silicon wafers using an electrolyte containing hydrofluoric acid. However, these films were of relatively little interest at the time, and it has not changed substantially until the beginning of the 1990s. Its development was first justified for technological reasons, in particular, localized isolation in microelectronics. In 1971, Watanabe and Sakai, demonstrated the first application of PS in electronics, the so-called full isolation by the porous oxidized Si process (FIPOS), where the PS layers were used for device isolation in integrated circuits (Wanatabe *et al.*, 1975). In the 1980's the material has been demonstrated to be very-large-scale integration (VLSI) compatible with the full isolation by porous oxidized silicon (FIPOS) method developed for dielectric isolation (Unagami, 1980; Imai, 1981). In addition, in the 1980's, several studies of the optical properties of porous silicon were published and photoluminescence in the deep red near-infrared was detected at cryogenic temperatures (Pickering *et al.*, 1984).

In 1990, Canham, reported that if porous silicon is further etched in HF for hours after preparation, it emits bright red light when illuminated with blue or UV light. Longer etching in HF was demonstrated to lead to brighter photoluminescence at shorter wavelengths, which was ascribed to quantum confinement. Longer etching increases the porosity, which produces, on the average, smaller nanocrystalline columnar structures. When the dimension of the columns decreases below 5 nm, the bandgap widens by quantum confinement in the conduction and valence bands and thus smaller columns produce larger bandgaps.

Porous silicon has been studied for the past decade: porous silicon formation studies, characterization of its structure and luminescence investigation have all been conducted (Pavesi *et al.*, 1993). Pavesi *et al.* (1995) first demonstrated that alternate PS layers of different porosities, i. e. different refractive indices, can be realized by

electrochemical etching using appropriate modulation of anodization time and current density. This technique resulted in a sharp optical emission having FWHM of about 15 nm and made possible the fabrication of PS microcavity (Pellegrini *et al.*, 1995; Reece *et al.*, 2002). PS usually emits red-green light, and does not emit blue light even when the crystallite size drops well below 3 nm (Sun *et al.*, 2005). Several models have been proposed to explain its PL, the most suggested are quantum confinement (Canham, 1990; Wilson *et al*., 1993), surface state (Koch *et al*., 1993), and oxide defects (Prokes, 1993). On the other hand, in addition to the interesting fundamental scientific problems concerning the PL mechanism, PS has offered us considerable technological interest because it may allow the convenient incorporation of optical elements into Si integrated circuits. The incorporation of a stable and efficient luminescent PS element into a microelectronic circuit encourages the possibility of commercial applications significantly.

Regarding the PL of PS layers, thermal annealing treatments have been demonstrated to achieve strong and stable PL intensity (Tsai *et al*., 1991; Fischer *et al*., 2000). Further the laser heating effect similar to the annealing has been introduced (Prokes *et al.*, 1994; Salcedo *et al*., 2001). More recently, Fujiwara *et al*. (2005), observed a remarkable enhancement in PL intensity of PS by a factor of over 250 by laser irradiation.

On the other hand, it has been demonstrated that the luminescence features of PS are strongly affected by post treatments of the samples, for example, methanol exposure (Rehm *et al*., 1995), F_2 and H_2O exposures (Wadayama *et al*., 1998), and electro-deposited metal treatment (Rigakis *et al.*, 1996; Shi *et al.*, 2000). Furthermore, Zhao *et al*. (2005), has examined the enhanced mechanism of PL from chloride salt ion passivated PS. These recent works however, have shown that extra

complicated fabrication steps are required to maintain some important spontaneous emission characteristics from PS such as shorter wavelength, tunability of the emission wavelength, high intensity and stability of the PS structure.

In this work, we have modified the pulsed current etching technique to produce novel PS structures. In this technique, instead of using a dc current, a sequence of current pulses is used to form porous material. Porous silicon with controlled thickness has been successfully prepared using this technique which gives thicker and more uniform porous layers showing higher PL intensity (Qi *et al.*, 1994; Hou *et al.*, 1996; Liu *et al.*, 2003). The technique was also used to precisely control etching for processing nano-devices because the pulsed mode enables an extremely small etching rate of about 10^{-5} nm per pulse (Nanako *et al.*, 2006). As far as we know, we improved the use of the method to etch silicon for the PS formation and that the emission can vary over wide wavelength range. PL measurements of this method showed variety of emission wavelengths with strong intensity.

Optical spectroscopy is one of the most suitable methods for characterizing porous semiconductors. A study of the confinement of electrons in photoluminescence spectroscopy and the phonons in Raman spectroscopy gives quantitative estimation about the size of nanocrystallites and their distribution. Raman spectroscopy (Ashoken *et al.*, 1986) provides a rapid, nondestructive, and simple diagnostic method for determining the nanocrystal dimensions. Basically, confinement of the electrons and phonons in reduced dimensional systems leads to major modifications in their electronic and vibrational properties (Sui *et al.*, 1992). The vibrational modes, observed in the Raman spectra, are sensitive to the sizes. Different sizes of nanocrystallites will affect the shift, broadening, and lineshape of the Raman signal in different ways. Therefore, changes in the line broadening and

peak position of the optical phonon mode observed in the Raman spectra can be used as an indirect measurement for the shape and dimensionality of nanocrystallites (Yang *et al*., 1994). The Raman results indicated that phonon selection rules are relaxed in small crystallites due to the fact that phonons of wavelengths larger than the particle diameter cannot be sustained (Parayanthal and Fred, 1984).

1.3. Applications of Porous Silicon

The ease with which PS can be fabricated makes the material an attractive proposition for a progressive research area with wide range of novel ideas and applications for detecting different organic materials (Gaburro *et al.*, 2004), selective chemical sensors (Lewis *et al*., 2005), and solar cells (Menna and Tsuo, 1997; Aroutionuian *et al*., 2004). Porous silicon is considered to be a promising engineered material for chemical sensor applications due to its cost effectiveness and ease of integration with other Si-based devices. Recently, chemical sensors using PS layers have been reported, operating at room temperature up to 100 ºC (Polishchuk *et al.*, 1998; Iraji *et al*., 2004; Rahimi *et al.*, 2005) which is not possible for other semiconductor-gas sensors. The major barrier preventing commercial applications of PS is the instability of its native interface particularly a metastable Si–H termination. In typical porous silicon formation, the material's surface is passivated by hydrogen, and the required prolonged exposure to air for optimum surface oxidation thus inhibiting the ageing and stabilizing of the material.

Lewis *et al.* (2005) present a novel process for coating the devices using the electroless deposition of metals to provide enhanced sensitivity and selectivity to NO_x, CO, and NH_3. This process also allows the fabrication of the first room temperature tin-oxide facilitated CO sensor, and represents the first porous silicon

sensor to have sensitivity to CO. Tomioka *et al.* (2007) reported that the addition of oxidant H_2O_2 in HF solution results in a stable formation of PS layers on the front surfaces in a short time. More recently, Chen *et al.* (2007a) developed a practical oxidizing technique with ozone for the passivation of PS at room temperature. They achieved a complete replacement of Si-H_x coverage with Si-O_x film and Si-alkyl film. PS prepared with the aid of ozone shows enhanced PL intensity and better stability for aging in air. Here, we report on an innovative method for porous silicon formation; production of a rapid highly oxidized PS coupled with a large specific area, which could constitute a breakthrough in hydrogen gas sensing applications. In order to achieve this we have fabricated PS samples anodized in solution with and without the highly oxidizing H_2O_2.

1.4. Stability and Hardness of Porous Silicon

The use of PS has several drawbacks, determined by its brittleness and by the instability connected to the aging process i.e., the slow spontaneous oxidation of PS. Due to the ageing effect, the structural (Astrova *et al.*, 2002) and optical properties (Karacali *et al.*, 2003) of PS show continuous change with the storage time. The growth of the native oxide is completed approximately after a year (Petrova *et al.*, 2000). Various oxidation approaches, such as chemical oxidation (Rigakis *et al.*, 1997), anodic oxidation (Boukherroub *et al.*, 2002), conventional furnace oxidation (Chang *et al.*, 1999), rapid thermal oxidation (Chen *et al*., 1996), and aging oxidation (Fukuda *et al.*, 1997), were used to generate a more stable O-passivated surface to replace the unstable H-passivated surface to eliminate the aging problem. The oxidation methods are used in optical applications, such as optical waveguides, photo detectors, and photoluminescence components.

However, PS has another disadvantage; mechanical stability due to the high porosity and the difficulty of integration of the electrochemical etching needed to produce PS with the Si VLSI processing technology. A proposed solution to solve the problem of the mechanical stability of the porous layer has been the use of multilayered structures, in which the high-porosity active layer is sandwiched between two low-porosity supporting layers. This structure shows also improved luminescence stability, but a lower intensity (Tsybeskov *et al*., 2000). Morales *et al.* 2007, has studied the relation between porous layer thickness and its hardness. A slight decrement in the Vickers hardness was observed. Recently, Fang's *et al.* (2007), experimental results revealed that thermal conductivity (TC) and the hardness of as-prepared PS, exhibiting a strong dependence on the preparing conditions, decrease with increasing porosities. After oxidization at different temperatures, TC of oxidized PS decreases with increasing oxidation temperatures, whereas the hardness increases a lot. In this work, we present a method to improve the stability of porous silicon structure by electrochemical deposition of a silicon capping layer.

1.5. Porous GaAs

The reduction of dimension to nanometer sizes often results in dramatic changes in the optical and structural properties. Nanometer size III–V semiconductors are promising materials for applications in the field of electronics and photonics since quantum confinement effect in such materials modifies the band structure and leads to unique optical properties. Blue shift of the optical absorption spectrum and size dependent luminescence are some examples of the interesting properties exhibited by these nanostructures. The indirect gap semiconductors;

porous Si, SiGe (Del Cano *et al.*, 2004), SiC (Sangsig *et al.*, 2000), GaP (Ursaki *et al.*, 2002) structures have been widely analyzed. However, there are few reports of porous direct gap semiconductors; GaAs (Hao *et al.*, 1997; Lockwood *et al.*, 1999; Missaoui *et al.*, 2007) and InP (Liu and Duan, 2001; Che *et al.*, 2006). Direct gap semiconductors are currently being investigated in the form of porous layers using several techniques. Among these techniques, anodic etching remains one of the most versatile, due to its simplicity and low processing cost.

GaAs is the second most common semiconductor material with a direct band gap (1.424 eV) and a large exciton Bohr diameter (19 nm) (Nayak *et al*., 2004). It has some unique properties that make it ideal for use in applications that silicon is ill-suited for. Tiginyanu *et al.* (1997) reported the fabrication of porous structure by anodic etching of n-type GaAs in aqueous solution of H_2SO_4. They observed a porosity-induced LO phonon–plasmon decoupling, a breakdown of the polarization selection rules and a vibrational mode in the frequency region between the bulk TO and LO modes. Perrier *et al.* (2001) have fabricated the GaAs nanocrystals by the laser ablation. Photoluminescence spectra show PL peaks shift of about 870 meV to higher energies compared to bulk GaAs (1.515 eV at 10 K). They have shown that the increase in energy is due to the confinement effect of electron and estimated sizes around 6 nm. Mavi *et al*. (2004) have synthesized porous GaAs (π-GaAs) by laser-induced etching. They observed PL spectra from etched GaAs having two broad luminescence bands along with a red shift in comparison to a sharp band from the unetched GaAs. Raman measurements exhibit enhancement of first-order LO mode peak intensity in the etched sample along with line-shape asymmetry and shifting of mode towards lower frequency with increasing laser excitation energy. Recently, Zeng *et al.* (2006) prepared GaAs granular films by electro-chemical anodic etching

of n-type GaAs in HCl electrolyte at different temperatures. Raman spectra revealed marked redshift and broadening, which could be explained by phonon confinement model. In this work we present a correlated Raman and PL study of π-GaAs.

Difficulty in controlling the nano-scale structure and related properties of GaAs remains as the main challenges. This obviously requires correlating the parameters of the synthesis process with the resulting nanostructure. The pulse current electro-chemical approach, if it attains sufficiently high controllability at the nanometer-scale, seems to be a highly useful technique for etching compound materials. In this work we report for the first time the formation of π-GaAs by using pulse current anodization technique.

1.6. Objectives of the Thesis

The main objectives of this work are as follows:

1. To improve the electrochemically formed nanocrystalline porous Si (PS) in terms of uniformity, thickness, and nanocrystalline size.
2. To provide information associated with the optical and chemical properties of PS needed to accomplish light emitting and gas sensing devices, respectively.
3. To improve the stability of PS, both optically (aging effect) and mechanically (brittleness).
4. To improve the structure and optical properties of porous GaAs (π-GaAs) formed by electrochemical etching.

1.7. Outline of the Thesis

The outline of the thesis is as follows: Chapter 1 deals with a literature overview of the research on PS and π-GaAs since their discovery and introduces the state-of-the-art in the synthesis, and properties of these materials.

In Chapter 2 an introduction to nanostructured materials basics and the underlying theory that governs their unusual optical properties are explained, a general theory of luminescence and quantum confinement will be presented. The physics of the porous silicon and GaAs formation are discussed.

In Chapter 3, the experimental results for synthesizing and modifying PS structures and the different parameters of the process that influence on the final characteristics of the fabricated layers are discussed. The details of optical PL and FT-IR measurements are explained. Chapter 4 presents the experimental results for PS formed by the modified pulse current anodization method, the effects of pulse parameters will be explored.

In Chapter 5, the formation and optical characterization of GaAs nano-structures is discussed. Two different methods were used to form π-GaAs; the conventional method of electrochemical anodization using HF or HCl based solution, and pulse current electrochemical anodization. Finally, chapter 6 presents the conclusions of our work and suggests research for the future.

CHAPTER 2

PROPERTIES OF NANOSTRUCTURED MATERIALS

2.1. Introduction

In this chapter, a general theory of quantum confinement and luminescence will be presented. The porous silicon formation process is explained. This process consists of the electrochemical etching of silicon wafers in solutions based on hydrofluoric acid. Firstly, the electrochemical etching process is described and the different stages of the porous silicon formation are explained. The anodization requirements that influence on the final characteristics of the fabricated layers are also discussed and the porous silicon photoluminescence is briefly explained. The mechanism of pore formation in n-type GaAs is discussed too.

2.2. Basic Principles of Bulk Semiconductors

The valence band structure is much the same for many semiconductors and exhibits a maximum at the Brillouin zone center or Γ point (i.e., at wave vector k = 0) (Bettotti *et al.*, 2002). In general, E(k) has maxima or minima at zone center and zone boundary symmetry points, but additional extrema may occur at other points in the Brillouin zone (Peter and Manuel, 2001). In the case of Si, the lowest point in the conduction band occurs away from high symmetry points near the X point at the Brillouin zone boundary (along <001>), whereas in GaAs it occurs at the Γ point (Blakemore, 1985). The energy gap in a semiconductor is defined as the separation between this conduction band minimum and the valence band maximum at the Γ point. Semiconductors are therefore commonly divided into two distinct categories

depending on the nature of their energy band gap. For GaAs, the energy gap is classified as direct, because a transition can occur directly at k = 0 between initial and final states having the same wave vector. Correspondingly, because of the initial and final states in Si have different wave vectors; Si is termed an indirect band-gap semiconductor, as opposed to direct bandgap GaAs and their band structures are shown in Fig. 2.1 (Blakemore, 1985).

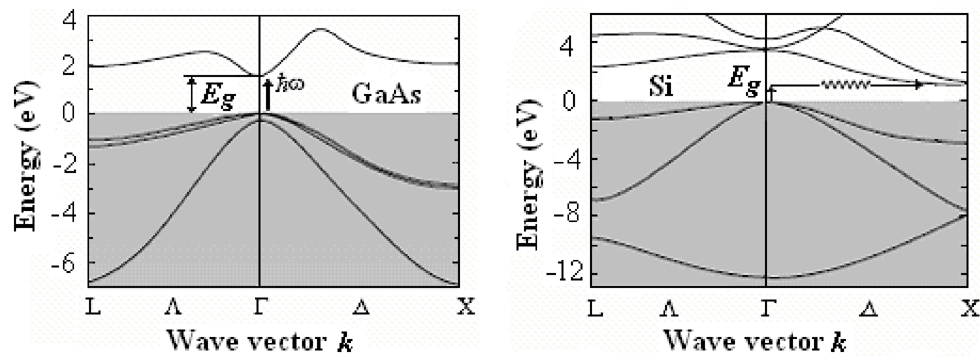

Figure 2.1: Schematic of the energy bands structure of GaAs and Si, the arrow indicates the lowest energy transition [After Blakemore, 1985].

2.3. Quantum Confinement in Nanostructured Materials

Beginning from a bulk, 3-D material (x, y, z), each dimension may be thinned conceptually to yield the three classes of quantum structures. Making the structure thin along the z-axis results in a 2-D layer called a quantum well. If thinned along a second axis (y-axis), a 1-D quantum wire is produced. Thinning along the final axis (x-axis) yields a 0-D structure called a quantum dot, as illustrated in Fig. 2.2(a-d) respectively. By considering that in bulk crystal a carrier is free to move in every direction, in a 2-D structure there are only two directions for the movement, while the third direction determines the quantum confinement direction. In a 1-D structure the free movement is possible in only one of the three directions, while in the two

remaining directions the quantum confinement occurs. In a 0-D structure there is a total confinement in each direction and the considered particle cannot move anymore. As a result of quantum confinement in the different directions there is a change in the wave function describing the behavior of electrons and holes, and consequently also the number of states per unit energy, i. e. the density of state (DOS), changes as a function of the energy E of the particle, as illustrated in Fig. 2.2.

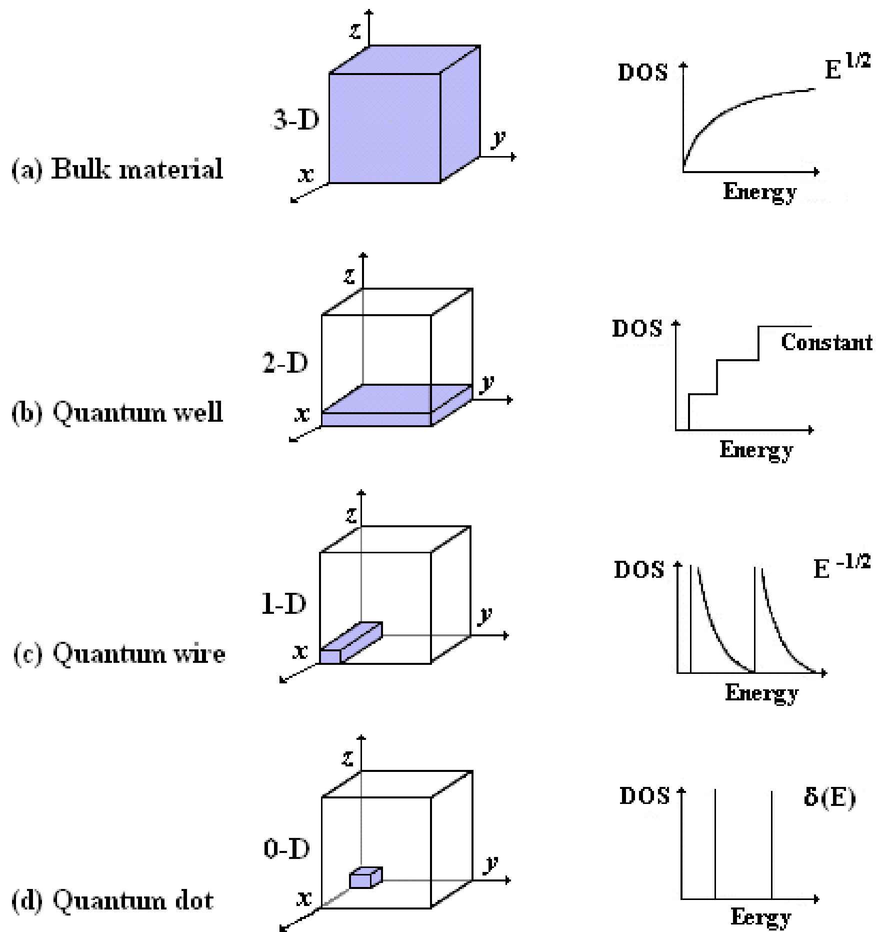

Figure 2.2: Schematic of the low-dimensional structure and the density of state (DOS) as a function of the energy for a particle controlled to move in the bulk (a), in a quantum well (b), in quantum wire (c), and quantum dot (d) [After Hens *et al.*, 2002].

In the case of a bulk material, the density of states increases with the energy of the particle following a parabolic law, being the DOS proportional to $E^{1/2}$ (Katz *et al.*, 2002). On the other hand, strong changes of the DOS are achieved when conduction electrons (valence holes) are spatially confined by reducing the size of the crystal to a few nanometers in one, two or three dimensions (Hens *et al.*, 2002). Quantum confinement in one direction determines a step-like increase of the DOS function with the energy. Totally different is the DOS function in the case of a 1-D nano-structure, where the number of state decreases following the $E^{-1/2}$ law as the energy increases. Finally, in the case of 0-D structure the function, in the ideal case, is formed by deltas marking the presence of discrete levels (Hens *et al.*, 2004).

A lot of theoretical work has been done in order to explain the size dependent optical properties of semiconducting nanocrystals, but all methods lead to an increase of the band-gap with decreasing crystallite size due to the carrier confinement (Delerue *et al.*, 1998). These methods are primarily based on the effective mass approximation (Sham and Nakayama, 1979; Qin and Jia, 1993), pseudopotential approaches (Brust *et al*., 1962) or the tight binding scheme (Slater and Koster, 1954). Among the various models for the size induced band gap expansion the "quantum confinement" theory (Canham, 1990; Sun *et al.*, 2001) which is based on the effective mass approximation (EMA) was recognized as the most successful model.

2.3.1. Effective mass approximation

Early theoretical studies have successfully applied the effective mass approximation to understand bulk semiconductor optical phenomenon (Lockwood, 1994). There is a fundamental difference between the calculations for the nanocrystals and the ones for the bulk. In the case of bulk materials, the EMA theory

treats the electron excited to the conduction band and hole created in the valence band as free particles, whose effective masses are determined by a quadratic fit to the curvature at the band minima (maxima) of the conduction (valence) band as illustrated in Fig. 2.3. The kinetic energies of electrons and holes can be expressed in terms of their effective masses, m_e and m_h (Lockwood *et al.*, 1996)

$$E = \frac{\hbar^2 k^2}{2m^*} \tag{2.1}$$

where, m^* is the effective mass of the charge carrier (electron or hole) and k is the wavevector. Direct band gap semiconductors have parabolic bands at the top of the valence band and the bottom of the conduction band. These bands are coincident in the k-space of the crystalline momentum (e. g. GaAs) (Lockwood *et al.*, 1996). On the other hand, in an indirect band gap (e. g. Si), the maximum of the valence band and the minimum of the conduction band appear not to coincide. Therefore, the EMA gives a good estimate of the band gap in large clusters of direct gap materials. The approximation is not accurate for states away from the point, or for indirect band gap semiconductors.

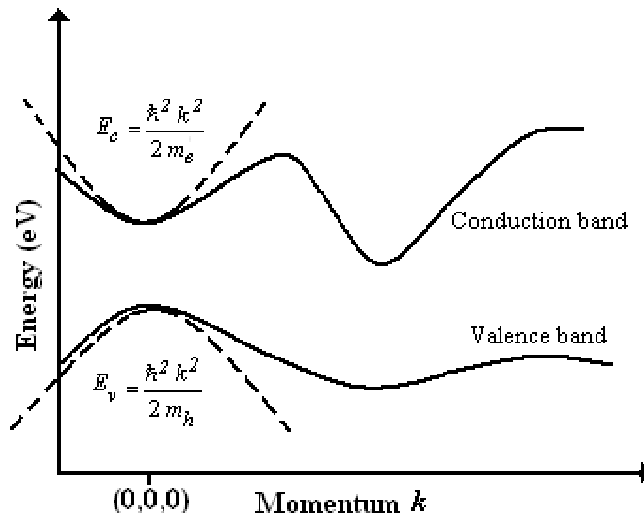

Figure 2.3: Effective mass approximation consists of quadratic fit to the valence maximum and conduction minimum [After Lockwood *et al.*, 1996].

Bulk model predictions break down however when the size of the crystal is less than the exciton's Bohr radius. For Si this is (4.3 nm) (Cullis *et al.*, 1997) and for GaAs is (19 nm) (Nayak *et al*., 2004). The Bohr radius of the exciton (electron-hole pair), is the natural physical separation in a crystal between an electron in the conduction band and the hole it leaves behind in the valence band. The size of this radius controls how large a crystal must be before its energy bands can be treated as continuous. Therefore, the exciton Bohr radius can rightly be said to define whether a crystal can be called a semiconductor quantum dot, or simply a bulk semiconductor (Lockwood, 1994). Crystallites with diameters smaller than this are said to be in the quantum confined (QC) regime (Wilson *et al.*, 1993).

Two regimes of exciton confinement must be distinguished. Kayanuma (1986) identified two limiting cases, depending on the confinement size *L* compared with the Bohr radius; weak confinement regime, this is the case when the crystalline size is small but still a few times larger than the exciton Bohr radius (Wilson *et al.*, 1993). In this regime, the relative electron–hole motion, and in particular its binding energy is essentially left unchanged. The exciton can be pictured as a particle moving inside the quantum dot with only little increase in energy due to the confinement. Strong confinement regimes occurs when the exciton Bohr radius is larger then the crystalline size of a quantum dot. In that case the relative electron-hole motion is strongly affected by the barriers.

Quantum confinement perturbs the energy levels of carriers in a crystal. The perturbation can be understood simply by reviewing the basic quantum mechanical problem of a particle in a box (Das and Melissinos, 1986). Using the effective mass approximation, an electron, with an effective mass, m_e, and a hole, with an effective mass, m_h, are confined in a one-dimensional infinite potential well. The potential as a

function of position for this problem is shown in Fig. 2.4. The particle is assumed to exist in region II so the particle is contained within a finite region of space by infinite potential barriers. A particle cannot penetrate these infinite potential barriers, so the probability of finding the particle in regions I and III is zero.

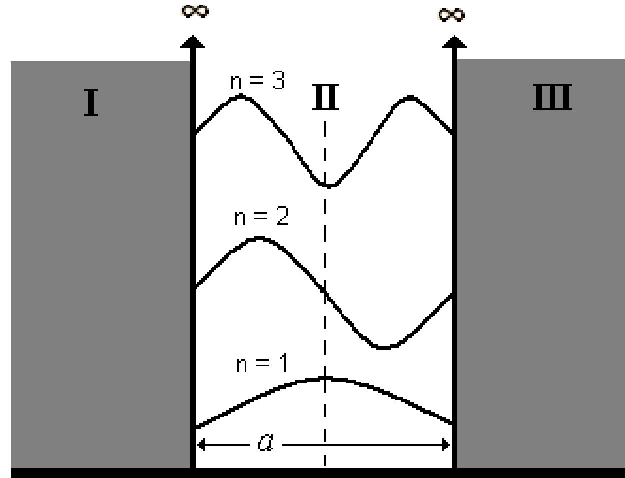

Figure 2.4: Schematic diagram of a quantum mechanical system by a particle of mass m confined in a one-dimensional box of length *a*. For the particle to be confined within region II, the potential energy outside (regions I and III) is assumed to be infinite [After Das and Melissinos, 1986].

The solution to the time independent Schrodinger equation yields discrete energy levels and the energy is inversely proportional to the square of the width of the well. Thus the band gap energy due to quantum confinement increases with respect to the bulk band gap energy as the width of the well decreases (Das and Melissinos, 1986),

$$E_g^{Confined} = E_g^{Bulk} + \frac{\hbar^2 n^2 \pi^2}{2a^2}\left(\frac{1}{m_e} + \frac{1}{m_h}\right) \tag{2.2}$$

where a is the width of the potential well, and n is the quantum number. Because of the confinement of both the electrons and the holes, the lowest energy optical transition from the valence to the conduction band increases in energy, effectively

increasing the band gap. The energy of the freely moving carriers is responsible for the band gap expansion and the width of the confined band gap grows as the characteristic dimensions of the crystallite decrease as illustrated in Fig. 2.5.

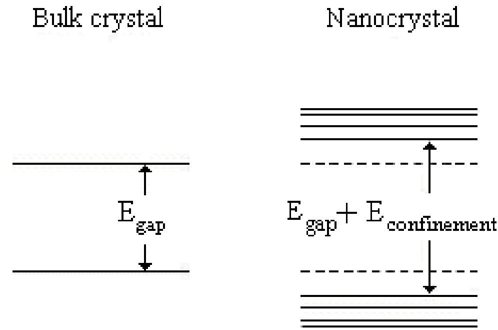

Figure 2.5: Confinement within nano-sized crystallite causes enlargement in the band gap energy, with respect to the bulk crystal.

2.3.2. Empirical pseudopotential method

Another method that has been applied is an empirical psedopotential theory (Brust *et al.*, 1962; Zunger, 2001), which has been used for nanoparticles by imposing a boundary condition on the pseudopotential solution for an infinite lattice (Rama and Friesner, 1991). There is better agreement with experiments compared to EMA, but the method does not include surface effects, as an infinite potential step is required at the surface. Yet, the surface of nanoparticles may influence or may even dominate the particle properties. Zunger and coworkers employed the semi-empirical pseudopotential method to calculate the electronic structure of Si, CdSe (Wang and Zunger, 1995) and InP (Fu and Zunger, 1997) quantum dots. Unlike EMA approaches, this method based on screened pseudopotentials allows the treatment of the atomistic character of the nanostructure as well as the surface effects.

2.3.3. Tight-binding method

Within the tight-binding (TB) approach, Slater and Koster (1954) described the linear combination of atomic orbitals (LCAO) method as an efficient scheme to calculate the electronic structure of periodic solids. It has extensively been employed to calculate electronic structures of various metals, semiconductors, clusters and a number of complex systems such as alloys and doped systems. Green's function recursion within the tight-binding approximation was also used to estimate bandgaps and exciton energies of nanoparticles (Lippens and Lannoo, 1989). The method models the atomic structure of clusters realistically and can be used to study surface effects.

2. 4. Light Emission from Silicon Nanostructures

Semiconductor nanocrystals just as bulk semiconductors are characterized by the structure of their conduction and valence bands as being direct or indirect. Direct semiconductor nanocrystals (e.g. GaAs, CdS) are characterized by having the minimum transition energy to prop up an electron from the valence band to the conduction band without a change in the electron momentum (the energy of this energy separation is known as the band-gap). For indirect semiconductors (e. g. Si), however, excitation at the band gap energy must be accompanied by a change in the electron's momentum (supplied by a phonon) (Bettotti, 2002). In the direct gap, an excited electron at the bottom of the conduction band can relax spontaneously back into a hole in the valence band by emitting a photon at the band gap energy (radiative recombination also called band-to-band recombination). Thus the probability of radiative recombination is high and the radiative lifetime is typically of the order of a few nanoseconds (Garbuzov, 1980). This electron-hole radiative recombination

process can only occur in Si if momentum is conserved, i.e., the excited electron wave vector must be reduced to zero. This, in pure Si, occurs via the transfer of momentum to a phonon that is created with equal and opposite wave vector to that of the initial state in the conduction band. Such a three-body process is quite inefficient compared with direct gap recombination, and yields very low internal quantum efficiency ($\eta i \sim 10^{-6}$) for Si luminescence (Hammond and Silver, 1980) (depending on doping). This is why Si is such a poor light emitter.

In the case of non-radiative recombination, as the electron moves from one energy band to another, its lost energy must take some other form, and the form of energy distinguishes two types of recombination (Shockley and Read, 1952):

2.4.1. Shockley-Read-Hall recombination

Shockley-Read-Hall (SRH) recombination (also called trap-assisted recombination) occurs when an electron falls into a "trap", an energy level within the band gap (E_T) caused by the presence of a foreign atom or a structural defect. Once the trap is filled it cannot accept another electron. The electron occupying the trap energy can in a second step fall into an empty state in the valence band, thereby completing the recombination process (Shockley and Read, 1952). One can predict this process either as a two-step transition of an electron from the conduction band to the valence band or also as the annihilation of the electron and hole which meet each other in the trap as shown in Fig. 2.6. The life time for the SHR recombination is at room temperature often of the order of 100 μs. This is much shorter than the radiative recombination life time for e-h pairs in silicon which is of about 10 ms above 20 K (Tamor and Wolfe, 1980), indicating that non-radiative recombinations are much more probable.